Purdue University
Purdue e-Pubs

Open Access Theses | Theses and Dissertations

12-2017

Additive Manufacturing of Energetic Materials and Its Uses in Various Applications

Trevor J. Fleck
Purdue University

Follow this and additional works at: https://docs.lib.purdue.edu/open_access_theses

Recommended Citation

Fleck, Trevor J., "Additive Manufacturing of Energetic Materials and Its Uses in Various Applications" (2017). *Open Access Theses*. 1275.
https://docs.lib.purdue.edu/open_access_theses/1275

This document has been made available through Purdue e-Pubs, a service of the Purdue University Libraries. Please contact epubs@purdue.edu for additional information.

ADDITIVE MANUFACTURING OF ENERGETIC MATERIALS AND ITS USES IN VARIOUS APPLICATIONS

A Thesis

Submitted to the Faculty

of

Purdue University

by

Trevor J. Fleck

In Partial Fulfillment of the

Requirements for the Degree

of

Master of Science in Mechanical Engineering

December 2017

Purdue University

West Lafayette, Indiana

THE PURDUE UNIVERSITY GRADUATE SCHOOL STATEMENT OF COMMITTEE APPROVAL

Dr. Jeffrey F. Rhoads, Chair

Department of Mechanical Engineering

Dr. Steven F. Son

Department of Mechanical Engineering

Dr. George T.-C. Chiu

Department of Mechanical Engineering

Approved by:

Dr. Jay P. Gore

Head of the Graduate Program

ACKNOWLEDGMENTS

I would like to thank my advisor and mentor, Dr. Jeffrey Rhoads for guiding me through both my undergraduate and graduate studies while at Purdue. I would also like to thank my friends on the research team for their moral support and for taking regular coffee breaks. Finally, thank you to Dr. I. Emre Gunduz for all of his help with experimental design and offering his expertise on 3D printing and video/imaging techniques.

This research is supported in part by Purdue University as well as by the U.S. Department of Defense, Defense Threat Reduction Agency through grant No. HDTRA1-15-1-0010 and is managed by Dr. Cathie Condron and Dr. Allen Dalton. The content of the information does not necessarily reflect the position or the policy of the U.S. federal government, and no official endorsement should be inferred.

TABLE OF CONTENTS

Page

LIST OF TABLES

LIST OF FIGURES

Figure Page

ABSTRACT

Fleck, Trevor J. M.S.M.E., Purdue University, December 2017. Additive Manufacturing of Energetic Materials and Its Uses in Various Applications. Major Professor: Jeffrey F. Rhoads, School of Mechanical Engineering.

The work discussed in this document seeks to utilize traditional additive manufacturing techniques to selectively deposit energetic materials. The goal was to gain a fundamental understanding of how to use commonplace 2D inkjet printing and 3D fused deposition technology to selectively deposit reactive materials. Doing so provides the ability to manipulate the geometry, as well as composition, of the energetic material during the manufacturing process. Achieving this level manipulation and control has shown to be nontrivial, if not impossible, using traditional manufacturing methods. The ability to change the geometry of the energetic material at will greatly increases the ability of these energetic materials to be integrated with a wide range of systems, such as transient electronics.

To create a transient electronic device, a destruction mechanism and an initiation system need to be integrated with electronic components. Experiments in this document investigate nanothermites for their ability to serve as this destruction mechanism. Nanothermites were prepared at various equivalence ratios and syringe deposited onto silicon substrates. The resultant destruction was shown to vary with the equivalence ratio of the material. A wide range of substrate destruction was demonstrated, varying from disintegration to only charring the wafer. Materials prepared near stoichiometric conditions were shown to disintegrate the silicon substrates completely. As the equivalence ratio was raised, less severe destruction was observed.

The ability inkjet print these nanothermites provides the geometric control necessary to incorporate them into electronic components. An ink formulation process was explored in an attempt to create a fuel and an oxidizer ink, which could be inkjet

printed simultaneously to create a nanothermite. Separate inks allow for the equivalence ratio, and therefore the resultant destruction, to be selectively tuned during the additive manufacturing process. Additionally, this gives the advantage of only needing two largely inert, shelf stable inks, instead of having to develop a new ink for every desired destruction level. Various candidate inks were formulated using different loadings and combinations of surfactants. Polyvinylpyrrolidone was shown to be the surfactant best suited for holding both aluminum and copper (II) oxide nanoparticles in suspension over time. These inks both showed reasonable shelf stability as well as viable reactivity when stoichiometric nanothermite samples were prepared using on-chip mixing.

With respect to 3D printed energetic materials, fused deposition methods were used to print a fluoropolymer based energetic material which could be used as a multifunctional reactive structure. A reactive filament comprising of a polyvinylidene fluoride (PVDF) binder with 20% mass loading of aluminum (Al) was prepared using a commercial filament extruder and printed using a Makerbot Replicator 2X. The printing performance of the energetic samples was compared with standard 3D printing materials using metrics such as bead-to-bead adhesion and the surface quality of the printed samples. The reactivity and burning rates of the filaments and the printed samples were shown to be comparable. This result is imperative for fused deposition modeling to be used as a viable manufacturing method of energetic materials.

In total, this document lays some of the groundwork necessary for additive manufacturing to be adopted as a viable method for the selective deposition of energetic materials. Going forward these methods can be used to integrate energetic materials in a manner not possible using traditional manufacturing methods.

1. INTRODUCTION

1.1 Background

1.1.1 Additive Manufacturing Techniques

In the past 25 years, additive manufacturing (AM) technologies, encompassing both 2D and 3D printing, have evolved from rapid prototyping techniques into legitimate manufacturing processes for functional parts and products. Several printing methods, such as fusion based material extrusion, vat photopolymerization, laser sintering, and even inkjet printing, have been well developed, and the knowledge base behind the printing of standard materials is comprehensive [1–3]. However, while such printing techniques have become commonplace, there is still significant work to be done in characterizing and implementing nonstandard materials, especially functional materials that serve a purpose beyond prototype development.

Ongoing research seeks to surpass using AM for its rapid prototyping and geometrical advantages by encompassing the printing of multifunctional materials. For example, AM has been shown to be a viable way to print functional electronic devices [4–6]. Inkjet printing has been used to print electronic circuits by selectively depositing an ink consisting of either a conductive polymer or metal nanoparticles suspended in a solvent [7, 8]. These 2D efforts have even been coupled with 3D printing to manufacture structures with integrated electronic components [9]. AM has also been used to make functional devices such as batteries [10]. Recent efforts have attempted to infuse additives into the traditionally used AM polymers to improve their functionality [11, 12]. Within fusion based material extrusion, significant efforts have focused on using these additives to improve the strength of the material [13, 14]. While there have been significant advances in the printing of functional materials over the past decade, some classes of materials still need to be studied to assess their

compatibility with AM. Due to the current limitations caused by traditional manufacturing techniques, one class of functional materials that would greatly benefit from AM is energetic materials.

1.1.2 Application of Energetic Materials

Energetic materials are combustible materials containing both a fuel and an oxidizer in the same material. This allows them to react in a variety of environments because no other reactants are necessary for deflagration, which improves their ability to be integrated into a system as a multifunctional material. Energetic materials can be classified by function as propellants, pyrotechnics or explosives [15]. Applications of propellants range from propellants for space applications [16] to microthrusters [17] and air bag initiators [18]. Pyrotechnics have been used in smoke producers, flares, and other military applications [19]. The performance of these energetic materials has been shown to be dependent on parameters such as geometry and material composition. Due to the geometrical flexibility offered by additive manufacturing, the combustion performance of these materials could be controlled by the printing process. Pairing this with on-demand printing capabilities would allow for samples to be functionally tailored for a given application in one manufacturing process.

1.1.3 Additive Manufacturing of Energetic Materials

The scope of the work described in this document looks to develop certain AM methods to encompass the printing of energetic materials. As previously mentioned, the geometric flexibility of AM could revolutionize the applications in which these energy dense materials can used. The first AM method that will be investigated is piezoelectric inkjet printing. As mentioned previously, inkjet printing with standard materials and even with some functional materials has been well characterized at this point in time. However, with regards to the inkjet printing of energetic material that can be integrated for use in a practical system, much work still needs to be done. To

date, the majority of work concerning the 2D printing of energetic materials has dealt with developing standards for trace vapor detection methods [20,21]. While these papers demonstrate the inkjet printing of energetic material, the deposited material is not used functionally in a system. Recent work in the inkjet printing of thermites has shown to deposit enough material for the thermite to achieve a self-propagating reaction [22,23], which allows for these materials to be used functionally in a system. Much of the inkjet printing discussed in this document employs the technology of piezoelectric inkjet printing to integrate nanothermite functionally into a system and determine its usefulness with transient electronics.

With regard to the 3D printed energetic materials, several methods have been attempted in order to achieve significant material deposition. Electrospray deposition (ESD) methods have been shown to be a viable method to deposit thin films of thermite [24, 25]. Further studies with electrospray techniques have incorporated a polymer binder to give mechanical integrity to the energetic material while maintaining significant reactivity [26]. Direct writing has demonstrated the ability to deposit energetic materials with complex sub-millimeter features [27–29]. While these techniques have proven to be robust methods for material deposition, there are still drawbacks that can be addressed. Some of these methods have limited geometric control and require a solvent for printing, which will only increases the time of manufacturing. One type of 3D printing that has been considered is fused deposition modeling (FDM), which does not require solvent. Fused deposition modeling works on the principle of having a material with a polymeric binder which is melted in the hot end of an extruder and deposited onto a substrate to make a part or sample [2]. Some studies have incorporated thermite additives into common 3D printing polymers such as ABS and have explored the combustion characteristics of these energetic polymers to determine their viability to be used with fusion based deposition techniques [30]. Due to the fact that FDM requires the melting of the material, only certain energetic materials are compatible due to safety concerns related to early onset reactions. The 3D printing efforts discussed in this document look to further the field of additive

manufacturing to encompass the 3D printing of functional reactive materials using fused deposition modeling. The bulk of the work discussed focuses on finding the "sweet spot" where a polymer based energetic material can be printed using FDM techniques while remaining chemically stable.

1.2 Project Scope and Goals

1.2.1 2D Inkjet Printing Efforts

There exists a pressing need to secure and control access to certain high-value electromechanical systems. In the event that one of these systems is compromised, there is an additional need to ensure that the device in question is rendered inoperable or to limit the possibility of the device being reverse engineered. The end goal of the inkjet printing efforts discussed in this document is to additively manufacture a transient electronic device by incorporating energetic material with MEMS. In order to create a transient electronic device, an initiation device as well as a destruction mechanism need to be incorporated into the same system. The project goal is to inkjet print a metallic bridgewire to act as an initiation device and then incorporate nanothermite, also by using inkjet printing, in order to create an all-printed transient electronic device. This device then could be used to destroy adjacent electronic components. Chapter 2 focuses on the destructive capabilities of aluminium bismuth (III) oxide nanothermite. The work specifically investigates how the resultant destruction caused by the nanothermite can be controlled by adjusting the equivalence ratio of the material. Adjustment of the equivalence ratio can be easily achieved during the additive manufacturing process using two component fuel and oxidizer inks, which are discussed in Chapter 3 of this document. The focus of Chapter 3 is the work that was completed as part of an ink formulation process that was used to develop nanothermite inks for inkjet printing. Various candidate inks were tested to determine their capability to stay in suspension, their viscosity, as well as how well they reacted when mixed together. The result was two candidate inks, one fuel and one oxidizer,

that could be used in a double nozzle inkjet printing system to reactively create a nanothermite. These two ink could then be used to integrate the nanothermite into an electronic device. Further work investigating the inkjet printing of the initiation system as well as the nanothermite has been completed with this project goal in mind, but will not be discussed in detail in this document [23, 31].

1.2.2 3D Fused Printing Efforts

The main goal of this work was to develop a safe process to 3D print an energetic material using FDM techniques; transforming raw materials into a functional energetic structure. In order for 3D printing to be accepted as a viable manufacturing process for energetic materials, the process must be safe and the end products must be comparable in performance and reliability to material manufactured using traditional methods. Chapter 4 of this document discusses the work done looking into both of these issues. A safe process is developed to additively manufacture a functional, fluorpolymer based energetic material. Energetic pellets are made from micron sized aluminum and polyvinylidene fluoride (PVDF) powders, which are then extruded into filament. This filament is then printed using a Makerbot Replicator 2X. Several tests are ran in order to show that the energetic performance of the 3D printed samples is comparable to unprinted materials. Important settings for maintaining this comparability are also discussed.

2. IMPLEMENTATION OF NANOTHERMITE FOR THE CONTROLLED DESTRUCTION OF SUBSTRATES

2.1 Introduction

The work in this chapter seeks to advance device protection methods by exploring the use of energetic materials to fracture silicon substrates through force production, rather than solely heat generation or chemical breakdown. Specifically, nanothermite materials were utilized to fracture representative substrates using a simplified support structure upon which an electronic device could be integrated. This method provides the benefits of the chemical methods highlighted below, but does so on a much faster time scale. The specific objective of this work is to investigate the destructive capabilities of nanothermites at different stoichiometries, with the aim of enabling future material synthesis and system design to be based on the desired level of substrate destruction. To this end, this work represents the first step towards an nultimate goal of our research team – to seamlessly integrate sensor and control electronics with selectively-deposited energetic materials, creating smart microelectromechanical transient devices, or SecureMEMS.

In prior literature, several attempts have been made to create a transient electronic device; however, most of these prior efforts either do not integrate the electronic destruction mechanism on the microscale or have other notable design drawbacks [32,33]. For example, one previously-reported method has shown that electronics can be rendered inoperable by chemically degrading them through selectively-released acids or corrosives [34, 35]. Likewise, another effort takes advantage of the substrate design, allowing for the mechanical destruction of the device [36]. Other efforts look to use energetic materials in order to destroy the electronic device via an exothermic reaction of the material [37, 38]. While each of these methods address the need for

a destruction mechanism in a transient electronic device, there are certain, notable limitations, specifically the time scale over which the destruction takes place and the input energy required to render the device inoperable. A particular current challenge is to quantify the ability of an energetic material to fracture a device. In this chapter, a quick, inexpensive test was developed that was able to characterize the substrate fracturing capability of selectively deposited energetic materials.

2.2 Material Preparation

2.2.1 Thermite Stoichiometry

Both aluminum copper (II) oxide nanothermites and aluminum bismuth (III) oxide nanothermites were prepared to test the destructive capabilities of the materials. The exothermic, stoichiometric reactions for both thermites are:

$$2\mathrm{Al} + 3\mathrm{CuO} \rightarrow \mathrm{Al_2O_3} + 3\mathrm{Cu}, \tag{2.1}$$

$$2\mathrm{Al} + \mathrm{Bi_2O_3} \rightarrow \mathrm{Al_2O_3} + 2\mathrm{Bi}. \tag{2.2}$$

We vary the equivalence ratio of the nanothermite in these experiments, effectively changing the reactive properties of the material in order to tailor the thrust generation, amongst other outcomes. The equivalence ratio is defined as

$$\phi = \frac{\left(\frac{n_{fuel}}{n_{oxidizer}}\right)_{actual}}{\left(\frac{n_{fuel}}{n_{oxidizer}}\right)_{stoichiometric}}, \tag{2.3}$$

where n is the number of moles of each reactant [39]. Samples of nanothermite were prepared at various equivalence ratios using the procedure detailed below in order to observe a range of destructive capabilities.

2.2.2 Nanothermite Preparation

To prepare the aluminum copper (II) oxide and aluminum bismuth (III) oxide nanothermites, either copper (II) oxide nanoparticles (Sigma Aldrich, 50 nm) or bismuth

(III) oxide nanoparticles (Nanophase Technologies Corporation, 38 nm) were mixed with aluminum nanoparticles (Novacentrix, 80 nm, 82% active aluminum) and suspended in dimethylformamide (DMF). First, the nanoparticles were weighed for the specified equivalence ratio amounts using an analytical scale and inserted into a 10 mL plastic syringe (BD, Slip Tip) [40]. Then, enough DMF was added to the syringe to make an 8% volumetric solids loading, and Airtech Flashbreaker 1 tape was placed over the tip of the syringe to prevent leaking. During mixing, the syringe plunger was inserted to the point of leaving about 1 mL of the syringe empty in order to allow room for mixing. The syringe was then loaded into a custom polytetrafluoroethylene (PTFE) holder and clamped on a LabRAM resonant mixer (Resodyn Acoustic Mixers, Inc., Butte, MT). The syringe was mixed at an 80% intensity for 16 min, with the PTFE holder being inverted at the 8 min mark [40].

2.2.3 Nanothermite Deposition

Immediately after the mixing cycle was complete, the syringe was removed from the mixing holder and clamped over a manual X-Y Stage. A 14 gauge syringe tip was placed on the syringe to improve deposition accuracy and repeatability. Silicon wafers of two different thickness, 300 μm or 500 μm (Ultrasil Corporation, Hayward, CA, <1 0 0> Orientation), were centered under the syringe tip on the X-Y stage. The plunger of the syringe was then pressed until one drop of suspended nanothermite was deposited onto the silicon wafer ($\simeq$ 33 μL). This volume approximation was based on the final mass of the nanothermite, which was an average of 4.25 mg across all of the samples. The deposited sample was then allowed to dry for 30 minutes under a heat lamp to ensure all of the solvent had evaporated.

2.3 Experimental Procedure

2.3.1 Substrate Destruction

The samples prepared using the methods detailed above were tested to assess their fracturing capabilities. The goal was to demonstrate a range of fracturing to the substrate for both silicon wafer thicknesses, varying from disintegrating the substrate all the way to not fracturing it at all. To achieve this destruction, the samples were placed on a 3D printed fixture simulating a simply-supported structure. The trough support fixtures were printed using a Makerbot Replicator Z18 3D printer and standard Makerbot PLA filament with a resolution 0.2 mm. A side view schematic of the experimental set up can be seen below in Figure 2.1. The square wafers, measuring 13 mm across, were centered over the trough with 11 mm between the supports. If the support was damaged during the course of experimentation, a replacement support was used to ensure consistent boundary conditions.

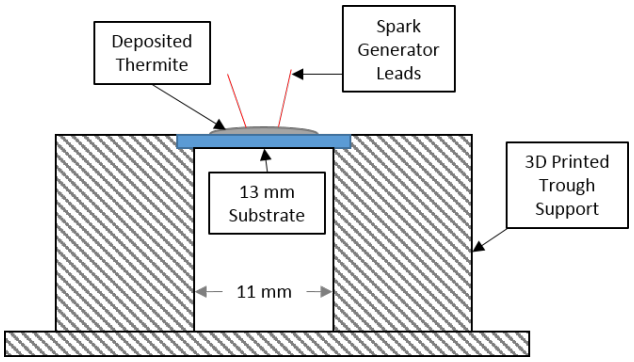

Figure 2.1. Side view schematic of the substrate destruction experimental set up.

The samples were ignited via spark ignition using a capacitive discharge unit (Information Unlimited, Amherst, NH), with the leads placed in contact with the sample. Due to the minimal contact between the leads and the substrate, the unit was assumed to not be assisting in the fracturing of the wafer. The samples were ignited on

the fixture inside of a clear acrylic box in an attempt to gather as many remnants of the substrate as possible. Videos of the reaction were also obtained using a BW Phantom Camera V 7.3 (Vision Research, Inc, Wayne, NJ) in a schlieren imaging set up in order to capture videos of any shock waves being produced. The schlieren imaging was performed using an Edmund Optics (71-013) system which featured aluminized spherical mirrors with a 6 in diameter and a 60 in focal distance. The aperture was set at f1/32 on a Nikon ED AF Micro Nikkor 200 mm 1:4D lens. Typically, a knife-edge is used to block the beam, but the lens properties allowed the camera to be placed such that the aperture could be used as a knife-edge. This generates a schlieren with more uniform contrast. The images were recorded at a frame rate of 88,888 frames/s.

2.3.2 Thrust Experiments

Thrust measurements of duplicate samples were performed in order to compare the trend of the fracturing data to the trends of the thrust production from the thermite reaction. The thrust measurements were taken using a Kistler 9215 force transducer (Kistler Holding AG, Barcelona, Spain) connected to a DPO 4034 1 MHz oscilloscope (Tektronix, Inc, Beaverton, OR) to record the thrust trace. A DET10A photo diode (Thor Labs, Inc, Newton, New Jersey) was used as an external trigger source. Once the reaction took place, the diode triggered the oscilloscope, to record the force from the transducer, as well as trigger the BW Phantom Camera V 7.3. Thrust measurements were taken using the 500 μm wafers. The layout of the thrust measurement system can be seen in Figure 2.2.

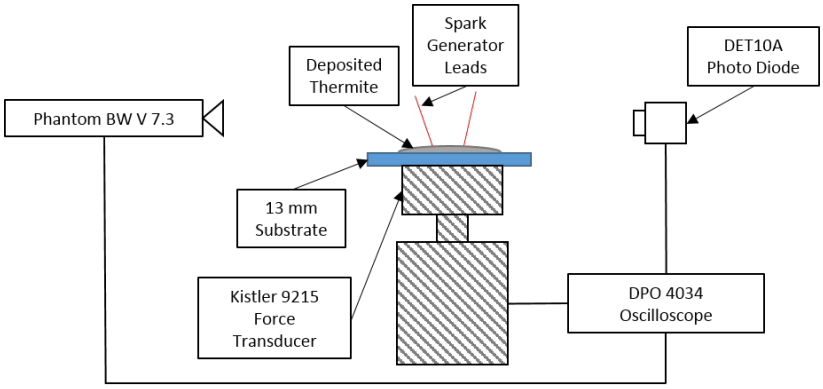

Figure 2.2. Schematic of the experimental set up used for thrust measurements.

2.4 Results

2.4.1 Substrate Destruction

Aluminum copper (II) oxide nanothermite was prepared and deposited at a stoichiometric ratio ($\phi = 1$) onto both the 300 μm and 500 μm thick silicon wafers. No fracturing of the substrate was achieved for either thickness. CHEETAH 7.0 thermochemical code calculations predicted that near $\phi = 1$ would yield maximum gas production. Given that this stoichiometry failed to fracture the substrate (for the volume of material used) and that it was predicted to yield maximum thrust, no other equivalence ratios were tested for the aluminum copper (II) oxide nanothermite.

Aluminum bismuth (III) oxide nanothermite was prepared and deposited at equivalence ratios of $\phi = 1$, 3, 4, 5, and 6 to achieve a range of fracturing. This range of equivalence ratios was chosen based on CHEETAH 7.0 constant pressure thermochemical calculations, which predicted a significant reduction in gas production across this range. For each equivalence ratio, 3 samples were prepared on wafers of both thicknesses. Four different qualitative fracture categories were used to describe the cleaving event. The first category, “Disintegrated”, was used to indicate that no significant shards of the substrate were collected. This type of fracturing would

be desirable due to the impracticality of piecing the device back together for reverse engineering for example. The next category, "Fractured", was used to signify that anywhere from 3-10 shards of the substrate were collected. "Cleaved" was used to designate if the reaction event left the wafer in exactly 2 pieces. "No Destruction" was used to categorize those wafers with no visible fracturing. The results of each fracturing event for the 300 μm and 500 μm thick silicon wafers can be seen in Tables 2.1 and 2.2.

Table 2.1.
Fracture event results obtained for aluminum bismuth (III) oxide nanothermite on 300 μm thick silicon wafers.

Equivalence Ratio	**Sample 1**	**Sample 2**	**Sample 3**
$\phi = 1$	Disintegrated	Disintegrated	Disintegrated
$\phi = 3$	Disintegrated	Disintegrated	Disintegrated
$\phi = 4$	Fractured	Disintegrated	Disintegrated
$\phi = 5$	Cleaved	Disintegrated	Disintegrated
$\phi = 6$	No Destruction	No Destruction	No Destruction

Table 2.2.
Fracture event results obtained for aluminum bismuth (III) oxide nanothermite on 500 μm thick silicon wafers.

Equivalence Ratio	**Sample 1**	**Sample 2**	**Sample 3**
$\phi = 1$	Disintegrated	Disintegrated	Disintegrated
$\phi = 3$	Cleaved	Disintegrated	Disintegrated
$\phi = 4$	Cleaved	Cleaved	No Destruction
$\phi = 5$	No Destruction	No Destruction	No Destruction
$\phi = 6$	No Destruction	No Destruction	No Destruction

Representative videos of each category of fracturing were also obtained using the same schlieren set up described earlier. Still frames of each video, along with representative before and after pictures of the silicon wafer, can be seen below in Figures 2.3 - 2.6. Figure 2.3 shows representative still frame images of a silicon wafer being disintegrated by the aluminum bismuth (III) oxide nanothermite. Due to the nature of the disintegration, no before and after pictures were included since a pulverized powder resulted. Note that the time stamp does not start exactly at start of the reaction ($t = 0$) due to the delay in the trigger from the photo diode. The substrate is reduced to dust within 30 μs of the start of the reaction, again leaving no significant remnants of wafer to be collected. A visible shock wave can be seen in the first frame of Figure 2.3, propagating in front of the gasses being produced. It should be noted that no visible shockwave was seen in the aluminum copper (II) oxide samples. This could imply a relationship between the presence of a visible shockwave and the fracturing produced, which is discussed later in this chapter.

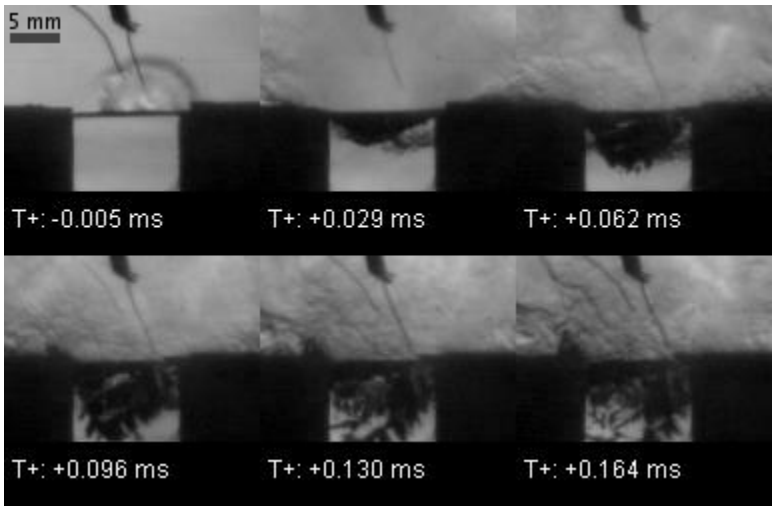

Figure 2.3. Still frame images obtained from a representative event in the "Disintegrated" fracture category. The event shown is of a 300 μm silicon wafter with aluminum bismuth (III) oxide sample at an equivalence ratio of $\phi = 3$.

Figure 2.4 shows the representative event of a sample which is categorized as "Fractured". In this scenario, 3-10 identifiable pieces of the substrate were collected. Still frames of the event along with before and after pictures of the substrate are included. The fracturing of the wafer occurred over a much larger time scale when compared to the "Disintegrated" category, taking almost 200 μs for significant damage to be noticed. A shock wave is also present in the first frame of Figure 2.4. This type of fracturing leaves much larger remnants of the wafer behind, opening the possibility for it to be pieced back together. However, some of the smaller pieces needed to reconstruct it entirely could not be collected.

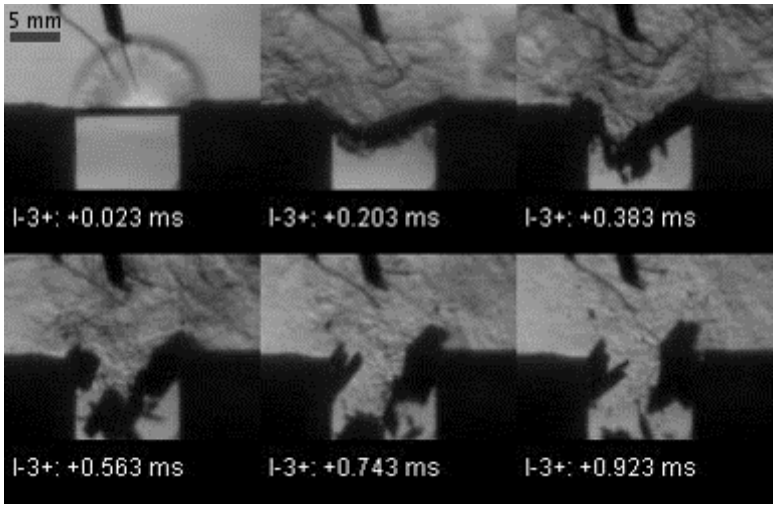

(a)

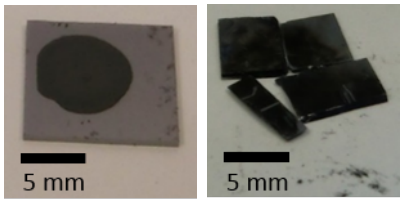

(b) **(c)**

Figure 2.4. (a) Still frame images obtained from a representative event in the "Fractured" fracture category. The event shown is of a 300 μm silicon wafter with aluminum bismuth (III) oxide sample at an equivalence ratio of $\phi = 4$. (b) An image of the nanothermite on silicon sample prior to ignition. (c) An image of the nanothermite on silicon sample following the event.

Figure 2.5 shows the representative event of a sample which is categorized as "Cleaved". In this scenario, only one line of fracture resulted from the reaction of the nanothermite. Still frames of the cleaving event along with before and after pictures of the substrate halves are included. The time scale of the fracturing is comparable to the "Fractured" scenario, once again taking approximately 200 μs for cleaving to be noticed. It should also be noted that no visible shock wave can be seen in Figure 2.5, implying that a shock wave is not necessary for fracturing to occur. While the entire

substrate was able to be reconstructed (no small fragments), this type of damage could be useful if the electronic device to be secured needed to be rendered inoperable, but there was no need to protect the information on it or prevent reverse engineering.

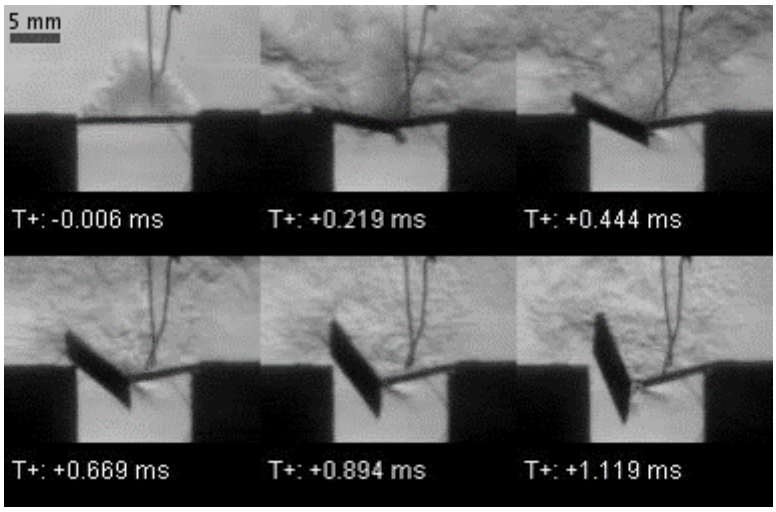

(a)

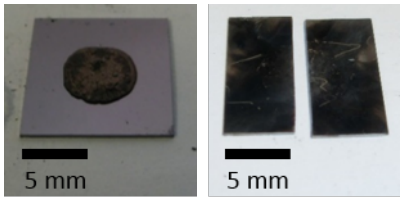

(b) **(c)**

Figure 2.5. (a) Still frame images obtained from a representative event in the "Cleaved" fracture category. The event shown is of a 500 μm silicon wafter with aluminum bismuth (III) oxide sample at an equivalence ratio of $\phi = 4$. (b) An image of the nanothermite on silicon sample prior to ignition. (c) An image of the nanothermite on silicon sample following the event.

Figure 2.6 shows the event of a sample which is categorized as "No Destruction". In this scenario, no fracturing of the wafer occurred during the reaction. Still frames of the representative event along with before and after pictures of the charred wafer can be seen below. Significant charring was left on the substrate after the reaction

took place. This scenario could be beneficial via heating or shorting a electronic device, which has been shown to be effective in prior work [37].

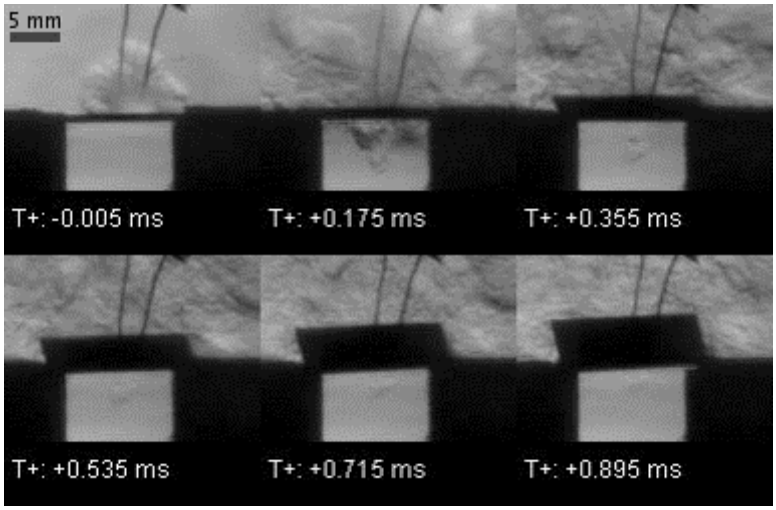

(a)

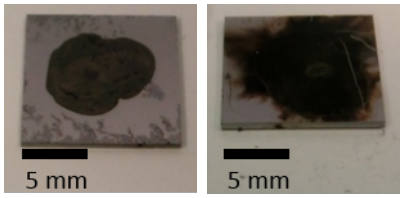

(b) **(c)**

Figure 2.6. (a) Still frame images obtained from a representative event in the "No Destruction" category. The event shown is of a 500 μm silicon after with aluminum bismuth (III) oxide sample at an equivalence ratio of $\phi = 4$. (b) An image of the nanothermite on silicon sample prior to ignition. (c) An image of the nanothermite on silicon sample following ignition.

2.4.2 Thrust Measurements

Thrust generation measurements were taken at each of the equivalence ratios considered to assess the trend between the level of substrate fracturing and thrust generation. Figure 2.7 shows a representative thrust trace. Slight trigger delays from

the photo diode result in the visible ignition event starting before $t = 0$. Oscillations in the signal can be attributed to the ringing of the test stand at its natural frequency. Figure 2.8 shows the average peak thrust of 5 samples of each equivalence ratio with the error bars representing the maximum and minimum peak thrust of the respective data set. As the equivalence ratio is increased, the average peak thrust decreases significantly to a point where there is no significant thrust generation at $\phi = 6$. The trend of the thrust reduction correlates with the reduction of fracturing, as might be expected.

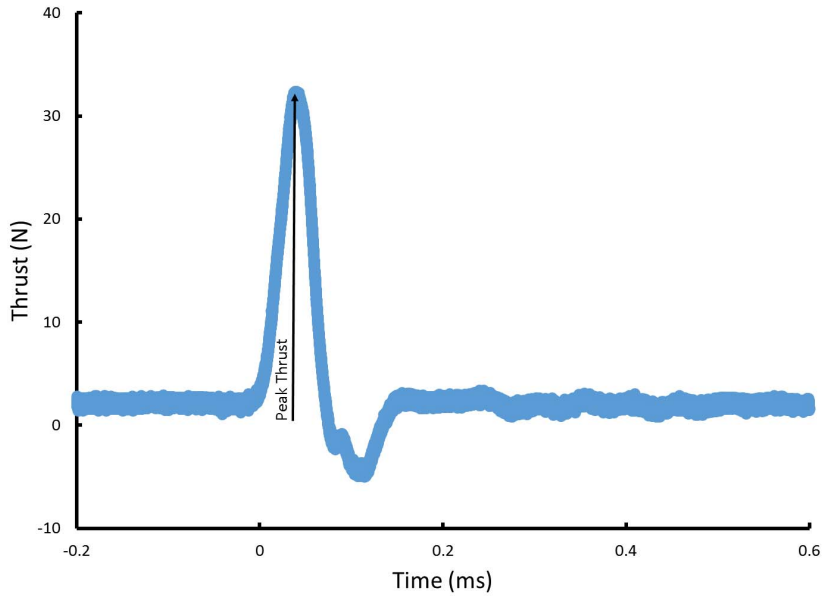

Figure 2.7. A sample thrust trace from an aluminum bismuth (III) oxide nanothermite sample with an equivalence ratio of $\phi = 4$.

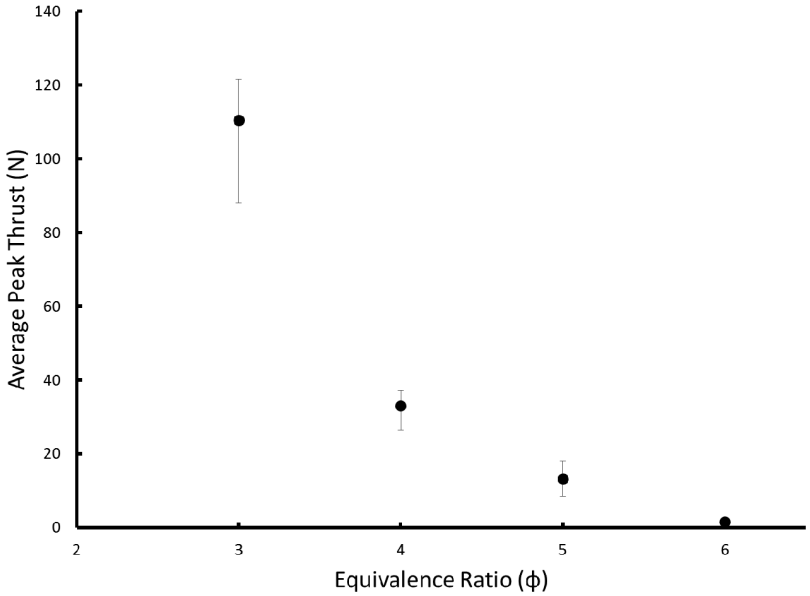

Figure 2.8. A plot of measured thrust versus nanothermite equivalence ratio for aluminum bismuth (III) oxide.

Thrust generation comparable to the $\phi = 5$ aluminum bismuth (III) oxide nanothermite was achieved using $\phi = 1$ aluminum copper (II) oxide nanothermite but resulted in "No Destruction". This can be an indication that other factors, in addition to the peak thrust generated, are causing the fracturing. One possible factor could be associated with the time scale over which the reaction takes place. Due to the reaction speed of the aluminium bismuth (III) oxide nanothermite, a shock wave is generated at the lower equivalence ratios (ϕ = 1-4). This shock wave was not seen in the videos of the aluminum bismuth (III) oxide reactions at the higher equivalence ratios (ϕ = 5-6), likely indicating the reaction is slowing down as the equivalence ratio is increased. Still frames from the videos of these shock waves are highlighted in Figure 2.9. Even though both reactions are shown at about the same point physically with the reactions reaching the end of the sample, the $\phi = 3$ sample is reacting approximately 5 times as fast as the $\phi = 6$ sample based on the time stamps of the

frames. The time stamps were adjusted so $t = 0$ correlates to the start of the visible reaction.

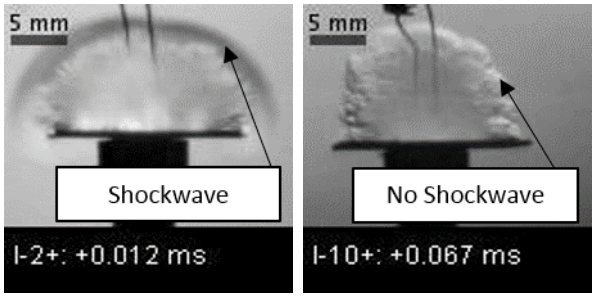

(a) **(b)**

Figure 2.9. Still images comparing (a) a representative $\phi = 3$ aluminum bismuth (III) oxide nanothermite ignition event to (b) a representative $\phi = 6$ aluminum bismuth (III) oxide nanothermite ignition event.

2.5 Conclusions

The work in this chapter details a quick, inexpensive test that can be used to characterize the effectiveness of a given energetic material to fracture a substrate. Small amounts ($\simeq 3.5$ mg) of aluminum copper (II) oxide nanothermite were tested to assess the material's destruction capabilities but resulted in no silicon wafer fracturing. In contrast, small amounts ($\simeq 3.9$ mg) of aluminum bismuth (III) oxide nanothermite were shown to be effective materials for the fracturing of silicon wafers. Nanothermites were deposited at various stoichiometries onto two different silicon wafer thicknesses, resulting in various forms of destruction. The destruction ranged from disintegrating the substrate to not fracturing the substrate at all for the aluminum bismuth (III) oxide system. This data was compared with thrust measurements. As expected, as the equivalence ratio was increased, less thrust was generated, resulting in correspondingly less fracturing of the substrate. This demonstrates the ability to selectively limit the destruction of a substrate via tailoring of the equivalence ratio of the deposited nanothermite. The fracturing resulting from the nanothermite reaction can be used

to disintegrate a MEMS or microelectronics device or render it inoperable. Future steps toward the project goal of creating a transient electronic device would require integrating the energetic material with a sensing and initiation capability, as well as improving the deposition of the energetic material, which has shown to be feasible using piezoelectric inkjet printing [23, 31]. The following chapter details an ink formulation process which would give the ability to integrate nanothermites into the electronics, as well as vary the stoichiometry, all during the inkjet printing process.

3. FUEL AND OXIDIZER INK FORMULATION FOR DOUBLE NOZZLE REACTIVE NANOTHERMITE PRINTING

3.1 Introduction

When trying to print any ink containing metal or metal oxide particles, it is vital to ensure that the ink will act as a stable suspension over the course of printing. If not, the particles could agglomerate causing sedimentation in the ink reservoir or clogging of the inkjet nozzle [41]. It is believed that the nanoparticles that are being suspended in these inks tend to agglomerate due to the surface effects of the nanoparticles. One approach to overcoming such agglomerations is to add a surfactant to the ink in an attempt to change the way the particles interact with one another. Two surfactants used commonly in the literature in the area of ink synthesis are polyvinylpyrrolidone (PVP) and cetyltrimethylammonium bromide (CTAB) [42, 43]. In some cases, two surfactants, acting as cosurfactants, have been shown to be effective. The work in this chapter lays out a strategic process for creating a stable ink suspension for both a fuel and an oxidizer ink that can be used in a two component, or double nozzle, reactive inkjet printer [23]. Various inks with different loadings of surfactant are tested for their compatibility with the nanoparticles. An optimum surfactant loading is found for the tested formulations, which resulted in a stable ink that serves as a viable option for printing.

3.2 Preparation of Nanothermite Ink Components

Both copper oxide nanoparticles (Sigma Aldrich, 50 nm) and aluminum nanoparticles (Novacentrix, 80 nm, 82% active aluminum) were suspended in dimethylformamide (DMF) at a 2% volumetric solids loading for the purposes of double nozzle thermite printing. Two surfactants, cetyltrimethylammonium bromide (CTAB) (MP

Biomedicals, Product 0219400480) and polyvinylpyrrolidone (PVP) (Sigma Aldrich, Product 437190) were added at various loadings and combinations in order to determine the optimal surfactant loading for ink performance. Three different surfactant combinations were prepared for both inks. The combinations included an all PVP case, an all CTAB case, and a case at a 1:1 ratio of PVP:CTAB. All three of these combinations were tested at three different loadings of surfactant; 0.25, 0.50, and 0.75 wt% of the nanoparticles being suspended. An ink without any surfactant was also prepared in order to be used as a control. Table 3.1 below summarizes the naming convention for these inks. A or C represents whether the ink contained aluminum or copper oxide nanoparticles respectively.

Table 3.1.
Ink naming convention for different surfactant combinations and loadings.

	All PVP	**All CTAB**	**1:1 PVP:CTAB**
0.25 wt %	Ink A1 or C1	Ink A4 or C4	Ink A7 or C7
0.50 wt %	Ink A2 or C2	Ink A5 or C5	Ink A8 or C8
0.75 wt %	Ink A3 or C3	Ink A6 or C6	Ink A9 or C9

CTAB and PVP were dissolved in DMF at the appropriate levels, then added to 1.5 mL microcentrifuge tubes containing the appropriate mass of nanoparticles. The microcentrifuge tubes were then inverted to ensure the nanoparticles were in suspension before mounting them in an Branson 1800 sonicating bath. The inks were then mixed via sonication for 30 min in order to achieve a uniform distribution of the nanoparticles throughout the solvent.

3.3 Experimental Procedure

3.3.1 Sedimentation Testing

Sedimentation tests simply observe how an ink's nanoparticles fall out of suspension over time. Immediately after sonication, the inks were mounted in an isolated area and were not disturbed until the all of the nanoparticles fell out of suspension. Pictures were taken at certain time intervals in order to observe qualitatively when the nanoparticles were no longer in suspension. The purpose of this test was to see how long the inks would remain shelf stable. From the settling time, it can be inferred how well the surfactants are preventing the nanoparticles from agglomerating. If the nanoparticles are falling out of suspension, the ink is no longer shelf stable, which causes complications with printing [41].

3.3.2 Viscosity Testing

For viscosity tests, the viscosity of the inks was measured over time to ensure the viscosity would not vary through out the duration of printing. The viscosity was measured using a Rheosense microVISC viscometer immediately after sonication, 1 hr after sonication, and 4 hrs after sonication in order to simulate the beginning, middle and end of printing.

3.3.3 Reactivity Testing

In order for an ink to be deemed suitable for double nozzle printing, the surfactant loading could not have significantly weakened the reaction. If the reaction of the nanothermite were weakened to the point of preventing self-propagation, the material would lose its ability to be used functionally in a system. In order to test if on-substrate mixing would produce a viable thermite, the inks were deposited via micropipette onto silicon wafers in order to show proof-of-concept for pursuing double

nozzle reactive printing. It was determined that four layers of 5 μL of total solution would provide enough material for a self-propagating reaction. In each 5 μL layer, a stoichiometric ratio of copper oxide ink and aluminum ink, as defined in Equation (2.1), was deposited and allowed to dry before the next layer was deposited. Once all four layers were deposited, the samples were ignited via spark ignition and qualitative data on whether or not there was a successful ignition was obtained. Three samples were prepared for each fuel and oxidizer ink combination in order to test which inks resulted in stable nanothermite mixtures.

3.4 Results and Discussion

3.4.1 Sedimentation Testing Results

All ten of the aluminum inks, as well as all ten of the copper oxide inks, were observed over time in order to determine their shelf stability, and to assess agglomeration. The aluminum inks showed shelf stability of up to 28 days. This was the point at which the experiment was cut off due to all of the inks not showing any signs of significant sedimentation. As shown in Figure 3.1 below, ink A1 began to show signs of initial sedimentation; however, all of the other inks were shown to be suitable at a shelf life of 28 days.

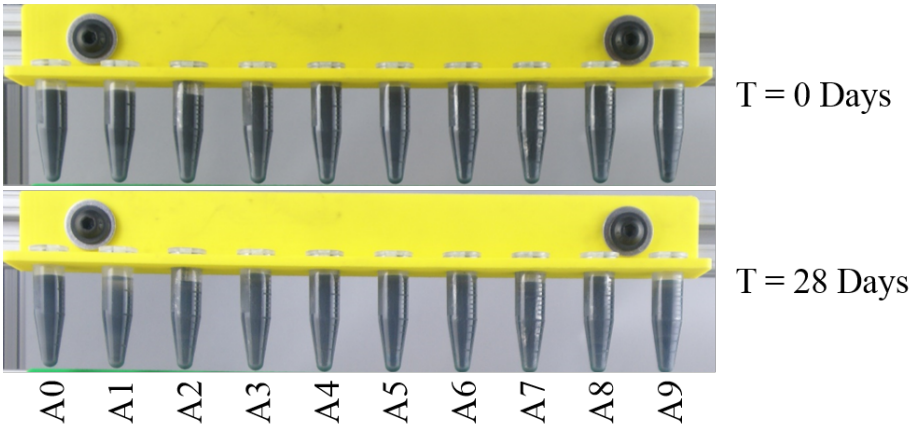

Figure 3.1. Images of candidate aluminum inks settling out over time.

The copper oxide inks settled out of suspension much faster. It was observed that inks C2 and C3 stayed in suspension the longest, lasting 24 hours before initial sedimentation was observed and 4 days for complete sedimentation. Given that inks C2 and C3 were comparable from a sedimentation perspective, it was inferred that 0.50 wt % is the upper bound beyond which adding more PVP would not result in a more shelf stable ink. The images shown below in Figure 3.2 show the copper oxide inks settling out over time, including the 24 hour picture showing when inks C2 and C3 begin to settle out of suspension.

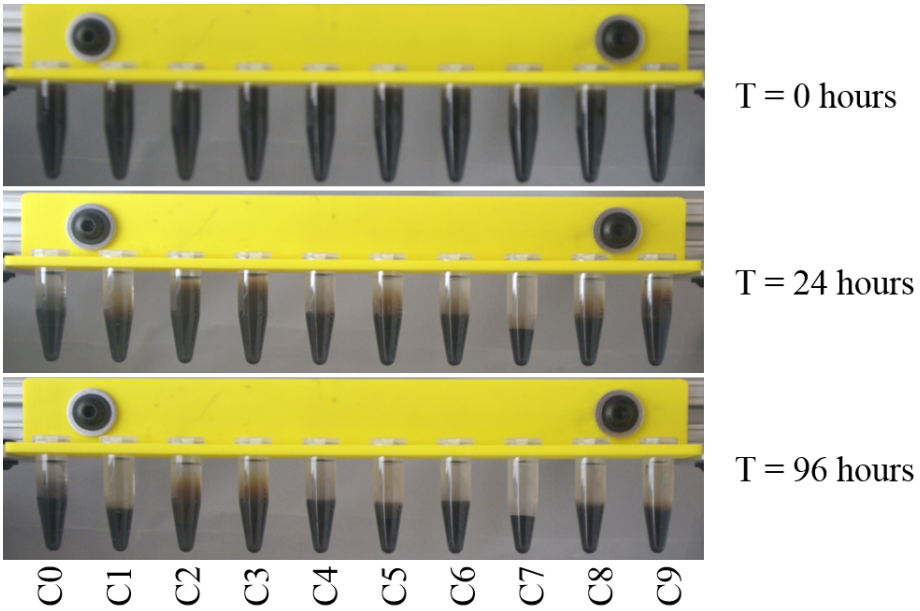

Figure 3.2. Images of copper oxide inks settling out over time.

3.4.2 Viscosity Testing Results

Viscosity measurements over time were collected for all ten of the aluminum and all ten of the copper oxide inks. While there were variations in the measurements between the aluminum inks and the copper oxide inks as well as over time, the variations were all within +/- 0.035 mPa·s of the measured value of DMF, 0.862 mPa·s. This was determined to be acceptable variations that would not drastically effect the performance of the ink over the duration of printing.

3.4.3 Reactivity Testing Results

From the sedimentation tests, as well as preliminary printing results, it was determined that C1 and C2, as well as A2, A5, and A8, were the best ink candidates for acceptable shelf life and stable printing. Stable printing was determined based on whether or not the ink could maintain stable droplet formation, qualitatively deter-

mined by side view imaging [31]. These inks as well as the control inks, A0 and C0, were mixed in all possible aluminum - copper oxide combinations in order to assess reactivity. Table 3.2 below shows whether or not the stoichiometrically deposited, 20 μL samples mixed well enough to achieve ignition.

Table 3.2.
Reactivity test results of pipetted thermite samples prepared via on-chip reactive mixing. 1 signifies ignition; 0 signifies no ignition.

	A0			**A2**			**A5**			**A8**		
C0	1	1	0	1	1	0	1	1	1	1	1	1
C1	1	0	0	0	1	0	0	0	0	1	0	0
C2	1	1	1	1	1	1	1	1	1	1	1	1

From the results, it can be seen that formulations containing ink C2 showed the best reactivity amongst the on-substrate mixed nanothermite samples. This could be due to the addition of PVP resulting in a more stable mixture, allowing for better on-substrate mixing. It should also be noted that the ignitions of the on-substrate mixed samples were qualitatively less robust than the acoustically mixed nanothermite reactions seen in previous chapters. This may be a result of sub-optimal mixing, small sample mass, or reduced intimacy between nanoparticles due to surfactant use. Qualitatively, the mixture of A2 and C2 showed the most robust reaction during the reactivity test.

3.5 Conclusions

It was clear that inks A2 and C2 were the top performers in each of the tests described above. Ink A2 was determined to be shelf stable for up to 28 days and was viable from viscosity standpoint. Ink C2 was shown to be shelf stable up to a day, which was the longest amongst the copper (II) oxide candidate inks. When mixed

together on-substrate, inks A2 and C2 formed a stable mixture which allowed for more intimate mixing when compared to the other on-substrate prepared samples. Due to this intimate mixing between the inks, a robust nanothermite reaction was achieved. Therefore, inks A2 and C2, each containing 0.5 wt% PVP, were selected to be used in the bulk of the main experimentation going forward for the double nozzle inkjet reactive printing of nanothermites.

4. ADDITIVE MANUFACTURING OF REACTIVE MATERIALS USING FUSED DEPOSITION METHODS

4.1 Introduction

The work in this chapter looks to further the field of additive manufacturing to encompass the 3D printing of functionally reactive materials. A process for how to safely create an energetic filament is presented along with pertinent printing settings that can be used with a Makerbot Replicator 2X. A polyvinylidene fluoride (PVDF) based filament is prepared with a 20% mass loading of micron-sized aluminum H3. The Al/PVDF filament was printed to produce samples to compare its printing performance with standard materials such as ABS. Metrics used for comparison include bead-to-bead adhesion, as well as the surface quality of the printed samples. Filament reactivity was quantified by measuring the burn rates of the filaments. Energetic performance was studied by performing differential scanning calorimetry (DSC) and thermal gravimetric analysis (TGA). This analysis was performed on both the printed and unprinted materials in order to ensure energetic performance did not degrade as part of the printing process. The presented work lays the technical foundation for the 3D printing of reactive materials using traditional fused deposition methods.

4.2 Methods and Materials

The fusion based 3D printing of a reactive material was achieved by using a three-step process to convert powder materials into a 3D printed sample. The three steps of the process included: pellet formulation of a polyvinylidene fluoride (PVDF) based energetic material; extrusion of a nominally 1.75 mm filament; and 3D printing of this filament using a Makerbot Replicator 2X 3D printer. PVDF was chosen for its suitably low melting point ($\simeq$175°C) and low decomposition onset temperature

($\simeq$375°C). H3 micron sized aluminum particles were chosen as a fuel source over nanoaluminum particles due to safety concerns during the filament extrusion process. When combined in the same material, aluminum will act as fuel with the fluorine in the PVDF acting as an oxidizer. A theoretical chemical equation describing how the aluminum reacts with the PVDF can be seen below in Equation (4.1). In order to get a better understanding of the products of this reaction, a thermochemical code, NASA CEA, was used for these materials at the ratios of aluminum and PVDF that were used during experimentation. A list of these products can be seen in Table 4.1. While trace amounts of several products were found using the thermochemical code, only the products containing more than 1% mole fraction were included. With these factors in mind, the following details how the 3D printing of Al/PVDF was achieved using fusion based material extrusion.

$$2\mathrm{Al} + 3\mathrm{C_2H_2F_2} \rightarrow 2\mathrm{AlF_3} + 6\mathrm{C} + 3\mathrm{H_2}, \tag{4.1}$$

Table 4.1.
Products of reaction for the Al/PVDF energetic material obtained from NASA CEA assuming 20% loading of aluminum by mass.

Product of Reaction	**Mole Fraction**
Carbon, C	0.4903
Hydrogen Flouride, HF	0.1955
Hydrogen Gas, H_2	0.1395
Aluminum Monofluoride, AlF	0.0795
Aluminum Fluroride, AlF_3	0.0705
Hydrogen, H	0.0155

4.2.1 Pellet Preparation

The first step in 3D printing the Al/PVDF energetic material was formulating pellets to be used in the filament making process. Agglomerate PVDF (Kynar 711) was dissolved in a co-solvent of acetone (Sunnyside Specialty Chemicals) and dimethylformamide (DMF) (Anhydrous 99.8%, Sigma Aldrich) to create a polymer precursor. For every gram of total material, 7 mL of solvent was used to create a precursor suitable for mixing in a digital sonifier (Branson Ultrasonics). A typical batch consisted of dissolving 0.8 g of PVDF in 2 mL of DMF and 5 mL of acetone. This solution was then mixed for 40 s in 4 intervals on a vortex mixer (Fisher Scientific) to ensure the agglomerate PVDF was completely dissolved. Then, 0.2 g of Al particles (H3, 4.5 μm diameter spherical particles, Valimet Inc.) was added to the solution prior to loading it in the digital sonifier (Branson Ultrasonics) such that the probe was 1 cm from the bottom of the 30 mL glass vial. The solution was mixed at an amplitude of 15% for 5 min. After mixing, the material was poured into a metal weigh tin to dry. After the material was dried for approximately 48 hr, the resultant 2 mm thick film was cut into pellet form (approx. 2 mm x 2 mm x 2 mm) to be fed into the filament extruder. The 20% loading aluminum was chosen as a starting point for this experimentation due to its viability from a reaction standpoint, as well as printing standpoint. It was shown that the Al/PVDF mixture can handle a loading of up to 50% aluminum by mass and maintain material integrity. However, the starting point for this experimentation was held at 20% in attempt to stay close to the ideal reactivity shown in Equation (4.1).

4.2.2 Filament Preparation

A filament extruder (Filabot, Original Filament Extruder) was used to extrude the Al/PVDF pellets into a 3D printable filament. When handling energetic materials, potential safety hazards are present and need to be addressed. In order to extrude the pellets into a filament, the Filabot extruder applies both heat and pressure to

the material using a feed screw and a heated chamber. In this part of the process, heat, pressure and confinement are applied to the energetic material. Therefore, as a precaution, the extrusion process was modified and operated remotely, being controlled from a separate room. This precaution was taken due to the dangerous effect confinement can have on an energetic reaction. If an accidental ignition occurred during extrusion, pressure caused by the produced gas would rise in the extrusion chamber, accelerating the reaction and cause destruction to the filament extruder. Because of this, energetic pellets were added to the extruder hopper followed by inert PVDF pellets. After 10 min of extrusion, excess amounts of the Filabot's extruder purge compound were added. This allowed for the energetic material to be extruded and then replaced by inert material, all while no direct human interaction occurred. During extrusion, the extrusion die and barrel were held at a constant 195°C, and the extrusion screw was operated at a rate of 35 rpm. Due to the extrusion process being controlled remotely, filament diameter was difficult to control. With no tension controller in place, the resultant filament was consistently oversized. In order to counteract this, a 1.60 mm nozzle was placed on the filament extruder in an attempt to keep the filament diameter below 1.75 mm, which is a design constraint of Makerbot Replicator 2X. After extrusion was complete, only sections with consistent filament diameter were used for experimentation ($\simeq$80% of the total filament extruded was used).

4.2.3 Sample Printing and Metrics

A variety of samples were printed using a Makerbot Replicator 2X for the characterization that will be discussed in the results section of this chapter. Consistent printing parameters were found to successfully produce samples with 100% infill with few defects. The key parameters identified were adjusting the layer height, as well as using a slower printing speed due to the low melt flow index of PVDF when compared with standard materials. The slower print speed allowed for the filament controller

to apply enough pressure to achieve the necessary bead size. It should also be noted that the filament diameter needed to be measured and adjusted in the software to account for the undersized filament sections. A complete list of the print settings used with the Makerbot Desktop Software can be seen in Figure 4.3.

4.3 Results and Discussion

For an energetic material to be used functionally, its combustion performance must be repeatable and well characterized. For the additive manufacturing of an energetic material to be successful using material extrusion techniques, process parameters need to be controlled carefully throughout all three steps of this process. If not, the variation of parameters could compound into unpredictable printing performance which would lead to inconsistent combustion performance, effectively limiting the functionality of the material. The results in the following sections highlight the importance of having a repeatable printing process and its influence on the combustion performance of printed energetic materials.

4.3.1 Energetic Performance of the Extruded Filaments

In order to ensure repeatable and predictable combustion performance of the printed samples, the energetic filament needs to be consistent from batch-to-batch, especially due to the hazards of processing large amounts of material at one time. Any filament inconsistencies would only be compounded by the printing process. Burning rate measurements have been widely used as a metric of combustion performance [44], and it is a suitable method for evaluating filament consistency. Therefore, three inch segments of filament from two different batches were burned and videos of the deflagration events were obtained in order to measure burn rates. To obtain these measurements, the filaments were aligned vertically, and secured at the base. Nichrome resistance wire (Consolidated Electronic Wire and Cable, 32 gauge) was then wrapped around the top of the filament 3 times. In order to ignite the filaments,

the nichrome wire was hooked up to a power supply (BK Precision, 1692 Power Supply) which supplied enough power to heat the nichrome wire and ignite the sample. A representative measurement is shown below in Figure 4.1 and the repeatability results are summarized in Table 4.2. Figure 4.1 shows a constant deflagration rate as the flame front propagates down the filament. This, paired with the results shown in Table 4.2, show that the filament burning rates are fairly repeatable within the different parts of the filament as well as from batch to batch. While there is a difference in the average burn rate from Batch 1 to Batch 2, this can be attributed to measurement method inaccuracies, as well as other parameter inconsistencies, such as a slight variance (+/- 0.15mm) in filament diameter across all of the samples.

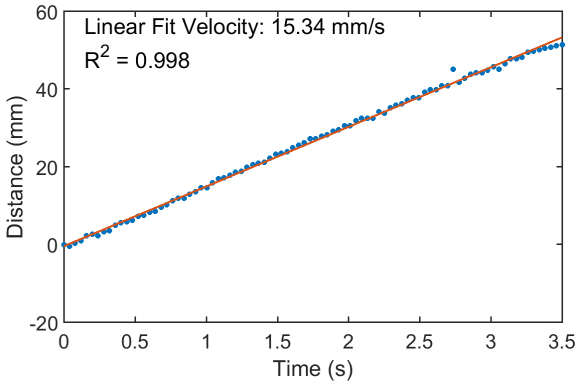

(a)

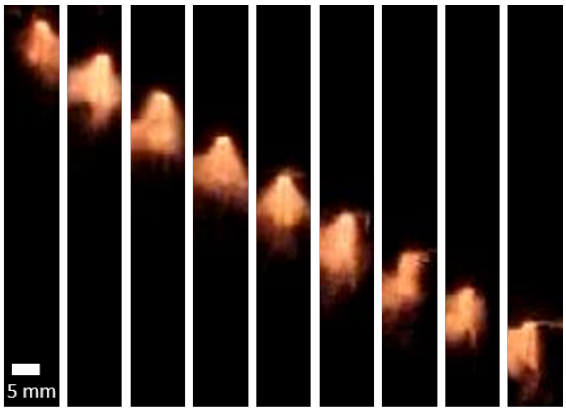

(b)

Figure 4.1. (a) The position of the flame front versus time obtained from images of the filament burning [shown in (b)]. (b) Still images from high speed videos showing the propagation of the flame front through the filament. The time step from image to image is 0.35 s.

Table 4.2.
A comparison of filament burning rates from two batches of pellets in order to investigate batch-to-batch repeatability.

Batch	**Sample Size**	**Avg. Diameter**	**Avg. Burn Rate**	**Std. Dev.**
Batch 1	6 samples	1.53 mm	18.7 mm/s	1.3 mm/s
Batch 2	5 samples	1.42 mm	15.0 mm/s	0.3 mm/s

4.3.2 Printing Performance

Once the batch-to-batch repeatability of the filaments was reasonably ensured, the energetic filament was printed using a Makerbot Replicator 2X. The desired infill of 100% without defects or gaps in the material was difficult to obtain using the standard printing settings. For this paper, 100% infill was chosen in an attempt to directly compare the combustion performance of the printed material with the combustion performance of the Al/PVDF filaments. Printing settings, such as layer height and print speed, had to be adjusted to obtain consistent printing of the 100% infill samples. The samples were printed with a 0.4 mm nozzle diameter and required a heated build plate. Due to the non-stick nature of the fluoropolymer base of the material, a contact promoting agent (glue stick, Elmer's Products Inc.) was used to ensure proper build plate adhesion. Due to the lower melt flow rate of PVDF as compared to ABS or PLA, the printing speed was lowered to maintain a consistent print bead. When 3D printing any material with 100% infill, it is imperative that precise, consistent bead dimensions are maintained in order to ensure no gaps occur in the printed sample. The table shown below in Figure 4.3 shows a complete list of the settings used to achieve proper infill of the samples.

Table 4.3.
Printing settings used for Makerbot Replicator 2X with Al/PVDF filament.

Device Settings			
Extruder Temperature	230 °C	Platform Temperature	120 °C
Travel Speed	10 mm/s	Z-Axis Travel Speed	23 mm/s
Minimum Layer Duration	5 s		
Extrusion Speeds			
All Print Speeds	10 mm/s	All Cooling Fan Speeds	50%
Infill			
Infill Density	100%	Infill Layer Height	0.2 mm
Model Properties			
Layer Height	0.2 mm	Number Shells	2
Roof Thickness	0.4 mm	Floor Thickness	0.4 mm
Coarseness	0.00010 mm	Fixed Shell Starting Point	Yes
Raft and Supports			
Raft	No	Supports	No
Right Extruder			
Filament Diameter	Set to Filament Used	Retraction Distance	1.3 mm
Retraction Speed	25 mm/s	Restart Speed	25 mm/s

Figure 4.2 shows images of the cross-sectional area of cylindrical samples printed with different print speeds and layer heights. The samples printed were cylindrical disks with a diameter of 10 mm and a height of 2 mm. The representative samples were sectioned using a low-speed diamond edge saw (Buehler Isomet 111280) and imaged on a digital microscope (HIROX KH-8700). The image in Figure 4.2(a) shows the cross section of an energetic sample that was printed with the recommended settings for a standard ABS filament. From the image, it can be seen that insufficient material was deposited which results in large gaps in the printed sample and poor bead-to-bead adhesion. The image in Figure 4.2(b) shows the cross section of a sample printed with adjusted settings that account for the different material properties of the PVDF based filament. The diagram in Figure 4.2(c) shows the orientation of the cross section images show in 4.2(a) and 4.2(b) as well as the approximate location. For this sample, a layer height of 0.2 mm and a print speed of 10 mm/s were found to deposit the requisite amount of material for a proper infill with few defects. It should be noted that if settings, such as layer height, were over-adjusted, smaller defects and gaps started to reappear due to excess material deposition.

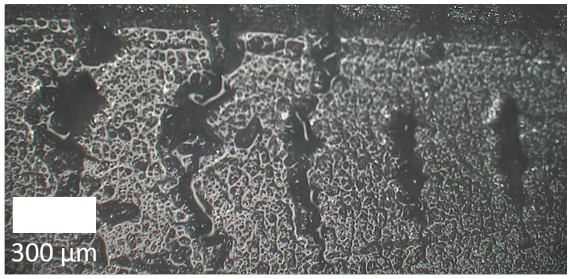

(a)

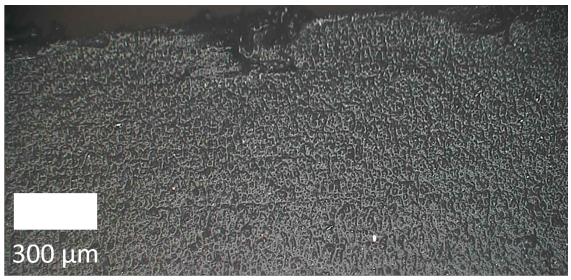

(b)

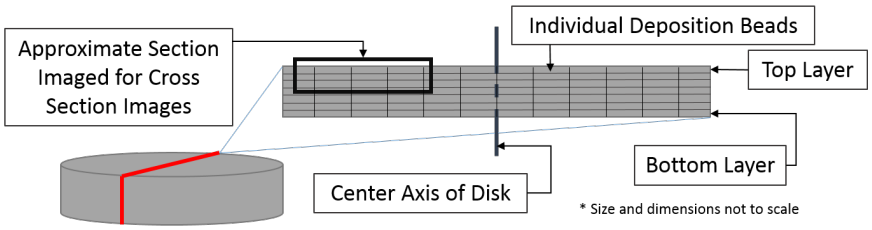

(c)

Figure 4.2. (a) The cross section of an Al/PVDF sample printed using the standard settings for an ABS filament. (b) The cross section of an energetic sample printed with adjusted settings to account for difference in material properties. (c) A diagram showing the orientation of the image, as well as approximate location on sample, of images (a) and (b).

The digital microscope was also used to take a 3D scan of the surface of the printed samples. Profiles of the 3D scans are shown in Figure 4.3 and indicate to some degree the surface finish of the printed samples. The surface finish of a standard printed ABS sample was included as a reference to show that the surface finish of the printed energetic material with proper settings is comparable to standard materials. The plot

shows that the gaps and defects shown in Figure 4.2(a) due to insufficient material deposition also resulted in significantly worse surface roughness. As expected, every 400 μm, which is the width of the nozzle, there is a trough in the materials. However, when printing settings were not adjusted to ensure proper infill in as in Figure 4.2(a), these troughs were up to 400% larger than the standard ABS samples.

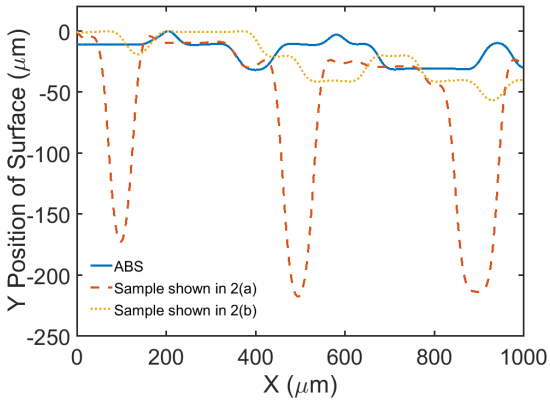

Figure 4.3. A plot showing the measured profiles of the surface of the 3D printed samples using different settings. An ABS sample was printed with standard settings. Also plotted are two energetic samples, one with standard settings and one with adjusted settings. Cross sections of these samples are shown respectively in Figure 2(a) and Figure 2(b).

4.3.3 Energetic Performance of the Printed Energetic Samples

One major concern with the additive manufacturing of energetic materials is how printing inconsistencies will affect the combustion performance. The suboptimal print settings and defects previously mentioned led to inconsistent combustion performance. Ideally, the material would have a thin flame front propagating through the material at a constant speed as in Figure 4.1. Figure 4.4 shows two deflagrations of printed samples, with settings and infill shown in Figure 4.2(a) (poor infill) and Figure 4.2(b) (good infill) respectively. The printed lines had a cross section of 1.6 mm by 1.6 mm in order facilitate comparison with the propagation speeds of the filaments. The same

ignition method that was used for the burning rate measurements of the filaments (described in Section 3.1) was used to ignite the printed samples. Figure 4.4(a) shows a thick flame propagating along the sample with poor infill and additional flame fronts spreading through defects and cracks. This resulted in an inconsistent deflagration and made burning rate measurements difficult to obtain. The flame front propagating through the sample in Figure 4.4(b) is more consistent and no flame spreading is observed. Comparison between Figure 4.4(a) and Figure 4.4(b) displays the importance of proper infill for reliable combustion performance. It should also be noted that most dark spots in the flame in Figure 4.4(b) are the products of the reaction entering the field of view. Once proper printing settings were determined, the combustion performance of the printed samples and unprinted samples were analyzed. Table 4.4 compares the results of the propagation speeds of the printed samples with the filament propagation speed and shows that the performance of the printed samples were very comparable (within the standard deviation) with the unprinted material. This implies that any defects or inconsistencies that may have resulted from the printing of the material were not significant enough to change the burn rate of the material.

Table 4.4.
A comparison of the burning rates obtained from FDM printed Al/PVDF samples and previously obtained filament burning rates.

Sample Type	**Sample Size**	**Avg. Size**	**Avg. Burn Rate**	**Std. Dev.**
Extruded Filament	11 samples	1.48 mm	17.03 mm/s	2.15 mm/s
Printed Sample	4 samples	1.52 mm	18.51 mm/s	2.20 mm/s

Provided proper infill, another concern with the fusion based 3D printing of any functional material is that heating the material past the glass transition temperatures necessary for deposition could result in a change of the functional properties of the material. Differential scanning calorimetry (DSC) and thermal gravimetric analysis

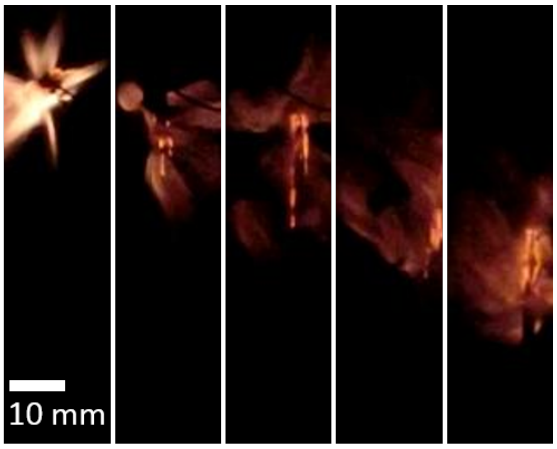

(a)

(b)

Figure 4.4. Still frames obtained at 0.35 s intervals showing the deflagration of a sample with (a) poor infill and (b) good infill.

(TGA) are common ways to evaluate the thermal response and reactivity of an energetic material. Figure 4.5 shows the DSC/TGA (SDT Q600, TA Instruments) results obtained for both filaments and printed material at a heating rate of 20 K/min and under OxyArgon flow. The plots in Figure 4.5 show heat flow (DSC) and weight percentage (TGA) as a function of temperature. Weight percentage tracks the weight of the sample in order to determine how much mass is lost to the gaseous products of the reaction. The heat flow tracks the amount of heat liberated or absorbed by the sample, where a positive heat flow shown here indicates exothermic reactions. There is one main exotherm in both the printed and unprinted materials which occurs around 575 °C. The temperature at which the main exotherm occurs, as well as the amount of heat generated, is similar between the printed and unprinted material. This implies that the melting and resolidifying of the material that occurs during printing is not significantly affecting the reactivity of the energetic material. Other points of interest include the slight endotherm that occurs at 170 °C which indicates the melting point of the PVDF polymer base of the material. Figure 4.5 shows significant decomposition starting to occur at 350 °C which leads to the onset of the main exotherm at approximately 375 °C. From this, it was determined that if the temperature of the material was kept below 310 °C during the printing and extrusion processes, no alteration of the material should occur.

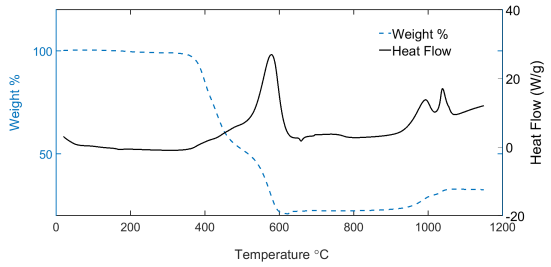

(a)

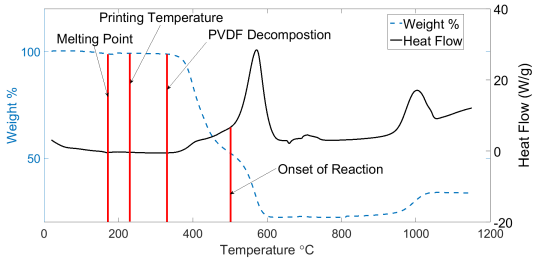

(b)

Figure 4.5. A plot showing the results of DSC and TGA analysis of the Al/PVDF material (a) before printing and (b) after printing.

Once proper settings were found to ensure reliable combustion performance, larger samples were printed. These samples were shown to have relatively good quality as compared to ABS samples as long as proper build plate adhesion was maintained. Figure 4.6 shows the Purdue University logo printed in both ABS and the Al/PVDF energetic material. The quality of the samples are comparable. Minor defects can be seen around the edges of the energetic sample. These are caused by the sample starting to detach from the build plate during the printing process. The energetic Purdue logo was able to deflagrate in a similar manner as the filaments and other printed samples. As long as build plate adhesion was maintained, the size and complexity of the printed energetic samples could be varied without any significant limitation.

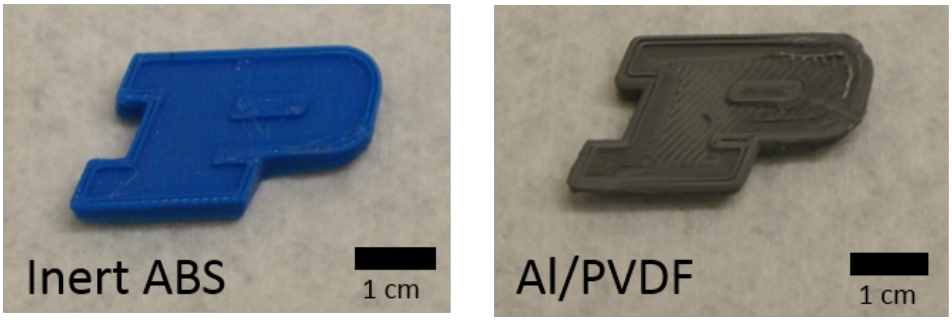

(a) **(b)**

Figure 4.6. Purdue University logo printed in (a) ABS and (b) Al/PVDF.

4.4 Conclusions

This chapter details a process to create an energetic filament safely and demonstrates the ability to print it successfully using a Makerbot Replicator 2X, while maintaining consistent combustion performance. A PVDF based filament was prepared with a 20% mass loading of micron-sized aluminum. The Al/PVDF filament was printed to produce reactive samples, and printing settings were optimized to improve the repeatability of the printed samples' combustion performance. The print quality of the energetic filament was shown to be comparable with standard materials such as ABS. Metrics used for this comparison included the optical analysis of bead-to-bead adhesion, as well as the surface quality of the printed samples. Batch-to-batch filament reliability was demonstrated by measuring the burning rates of 3 in sections of filament from two different batches. Energetic and thermal response was studied by performing differential scanning calorimetry and thermal gravimetric analysis on both the printed and unprinted materials, which showed that the energetic performance did not degrade due to the printing process. Additional work could include investigating how varying the printing infill affects the combustion performance of the reactive material. Also, intentional gaps, pockets, or channels could be printed into the sample in order to see what effect these have on the burn rate of the sample.

Other parameters in the pellet formulation process, such as the aluminum particle size (e.g. nanoscale Al could be considered) and solids loading, could be adjusted in order to increase the reactivity of the material since fuel-lean conditions were considered here. Further characterization of the energetic material is needed to integrate it as a functional material. Further characterization could include quantifying the sensitivity of the material using standard safety tests, such as sensitivity to impact, friction, and electrostatic discharge, as well as further characterization of the mechanical and reactive properties of the printed materials.

5. CONCLUSIONS

Two different additive manufacturing techniques, inkjet printing and fused deposition modeling, were shown to be viable methods for energetic material deposition. The ability to selectively deposit these materials increases their ability to be integrated with other systems as a functional material. Bismuth (III) oxide was tested for its viability to be used as a destruction mechanism in a transient electronic. It was shown that the amount of resultant damage to the substrate could be controlled by varying the equivalence ratio of the nanothermite during ink formulation. The range of destruction varied from completely disintegrating the wafer to only charring the surface. The ability to control the destruction based on energetic material composition gave motivation to create a separate fuel and oxidizer ink to be used with a piezoelectric inkjet printer. Separate inks comprising of aluminum and copper (II) oxide nanoparticles respectively were developed to determine their compatibility with inkjet printing. Various combinations and loadings of surfactants were tested for their ability to create a shelf stable ink without significantly affecting the reactivity of the final sample. PVP was shown to be the most effective surfactant, requiring a relatively small amount to improve the printing capabilities of the separate inks, while not causing significant impact on the reaction once the inks were reactively mixed on-chip. These inks would allow for the varying of the destruction previously showed to be tailored during the printing process.

Fused deposition modeling was shown to be a viable method of 3D printing reactive structures comprising of aluminum in a PVDF binder. A safe process taking micron sized aluminum and PVDF powders to 3D printed structures was developed. Various printing settings such as layer height and printing speed were shown to play an important role in ensuring proper infill in the printed materials. Once printed with

proper infill and no defects, the reactivity and burning rate the Al/PVDF structures were shown to be repeatable, as well as comparable to unprinted material.

REFERENCES

REFERENCES

[1] K.V. Wong and A. Hernandez, A Review of Additive Manufacturing. *ISRN Mechanical Engineering*, **2012**.

[2] B.N. Turner, R. Strong, and S.A. Gold, A review of melt extrusion additive manufacturing processes: I. process design and modeling. *Rapid Prototyping Journal* 20(3), 192-204, **2014**.

[3] B.N. Turner and S.A. Gold, A review of melt extrusion additive manufacturing processes: II. materials, dimensional accuracy, and surface roughness. *Rapid Prototyping Journal* 21(3), 250-261, **2015**.

[4] P. Calvert, Inkjet printing for materials and devices. *Chemistry of Materials* 13(10), 3299-3305, **2001**.

[5] A. Kamyshny and S. Magdassi, Conductive nanomaterials for printed electronics. *Small* 10(17), 3515-3535, **2014**.

[6] J.A. Lewis and B.Y. Ahn, Device fabrication: Three-dimensional printed electronics. *Nature*, 518(7537), 42-43, **2015**.

[7] H. Sirringhaus, T. Kawase, R.H. Friend, T. Shimoda, M. Inbasekaran, W. Wu, and E.P. Woo, High-resolution inkjet printing of all-polymer transistor circuits. *Science*, 290(5499), 2123-2126, **2000**.

[8] S.H. Ko, H. Pan, C.P. Grigoropoulos, C.K. Luscombe, J. Fréchet, and D. Poulikakos, All-inkjet-printed flexible electronics fabrication on a polymer substrate by low-temperature high-resolution selective laser sintering of metal nanoparticles. *Nanotechnology* 18(34), 345202, **2007**.

[9] D. Espalin, D.W. Muse, E. MacDonald, and R.B. Wicker, 3D printing multifunctionality: structures with electronics. *The International Journal of Advanced Manufacturing Technology* 72(5-8), 963-978, **2014**.

[10] E. Malone, M. Berry, and H. Lipson, Freeform fabrication and characterization of Zn-air batteries. *Rapid Prototyping Journal* 14(3), 128-140, **2008**.

[11] C. Esposito Corcione, F. Gervaso, F. Scalera, F. Montagna, A. Sannino, and A. Maffezzoli, The feasibility of printing polylactic acid–nanohydroxyapatite composites using a low-cost fused deposition modeling 3D printer. *Journal of Applied Polymer Science* 134(13), **2017**.

[12] J.W. Halloran, V. Tomeckova, S. Gentry, S. Das, P. Cilino, D. Yuan, R. Guo, A. Rudraraju, P. Shao, T. Wu, Photopolymerization of powder suspensions for shaping ceramics. *Journal of the European Ceramic Society* 31(14), 2613–2619, **2011**.

[13] S. Fu, X. Feng, B. Lauke, and Y. Mai, Effects of particle size, particle/matrix interface adhesion and particle loading on mechanical properties of particulate–polymer composites. *Composites Part B: Engineering* 39(6), 933-961, **2008**.

[14] A.R. Torrado Perez, D.A. Roberson, and R.B. Wicker, Fracture surface analysis of 3D-printed tensile specimens of novel ABS-based materials. *Journal of Failure Analysis and Prevention* 14(3), 343-353, **2014**.

[15] A.K. Sikder and N. Sikder, A review of advanced high performance, insensitive and thermally stable energetic materials emerging for military and space applications. *Journal of Hazardous Materials* 112(1), 1-15, **2004**.

[16] C. Fritz and O. Wilhelm, Solid rocket propellants. US Patent 3,429,264, February 25, **1969**.

[17] C. Rossi, S. Orieux, B. Larangot, T. Do Conto, and D. Esteve, Design, fabrication and modeling of solid propellant microrocket-application to micropropulsion. *Sensors and Actuators A: Physical* 99(1), 125-133, **2002**.

[18] J.B. Canterberry and D.A. Flanigan, Rapid burning propellant charge for automobile air bag inflators, rocket motors, and igniters therefor. US Patent 5,024,160, June 18, **1991**.

[19] S.M. Danali, R.S. Palaiah, and K.C. Raha, Developments in pyrotechnics (review paper). *Defence Science Journal* 60(2), 152-158, **2010**.

[20] E. Windsor, G. Gillen, M. Najarro, and A. Bloom, Use of inkjet printing technology to produce test materials for trace explosive analysis. *Microscopy and Microanalysis* 16(S2), 1572-1573, **2010**.

[21] R.M. Verkouteren, G. Gillen, and D.W. Taylor, Piezoelectric trace vapor calibrator. *Review of Scientific Instruments* 77(8), 085104, **2006**.

[22] A.S. Tappan, J.P. Ball, and J.W. Colovos, Inkjet printing of energetic materials: Sub-micron Al/MoO3 and Al/Bi2O3 thermite. Technical report, Sandia National Laboratories (SNL-NM), Albuquerque, NM (United States), **2012**.

[23] A.K. Murray, T. Isik, V. Ortalan, I.E. Gunduz, S.F. Son, G.T.-C. Chiu, J.F. Rhoads, Two-Component Additive Manufacturing of Nanothermite Structures via Reactive Inkjet Printing. *Journal of Applied Physics*. Submitted: August 10, **2017**

[24] H. Wang, G. Jian, G.C. Egan, and M.R. Zachariah. Assembly and reactive properties of Al/CuO based nanothermite microparticles. *Combustion and Flame* 161(8), 2203–2208, **2014**.

[25] H. Wang, J.B. DeLisio, G. Jian, W. Zhou, and M.R. Zachariah, Electrospray formation and combustion characteristics of iodine-containing Al/CuO nanothermite microparticles. *Combustion and Flame* 162(7), 2823-2829, **2015**.

[26] C. Huang, G. Jian, J.B. DeLisio, H. Wang, and M.R. Zachariah, Electrospray deposition of energetic polymer nanocomposites with high mass particle loadings: a prelude to 3D printing of rocket motors. *Advanced Engineering Materials* 17(1), 95-101, **2015**.

[27] F. Ruz-Nuglo, L. Groven, and J. Puszynski, Additive manufacturing for energetic components and materials. *In Proceedings 50th AIAA/ASME/SAE/ASEE Joint Propulsion Conference, Additive Manufacturing for Energetic Components and Materials*, Cleveland, OH, USA, **2014**.

[28] B.E. Fuchs, J.L. Zunino III, D.P. Schmidt, D. Stec III, and A.M. Petrock, Flexible detonator integrated with directly written energetics. US Patent 8,573,123, November 5, **2013**.

[29] J.L. Zunino III, D.P. Schmidt, A.M. Petrock, and B.E. Fuchs, Inkjet printed devices for armament applications. *Nanotechnology*, 542-544, **2010**.

[30] B. Clark, Z. Zhang, G. Christopher, and M.L. Pantoya, 3D processing and characterization of acrylonitrile butadiene styrene (ABS) energetic thin films. *Journal of Materials Science* 52(2), 993-1004, **2017**.

[31] W.A. Novotny, Inkjet Printing of Metallic Bridgewires, Master of Science in Mechanical Engineering Thesis. *Purdue University*, August **2017**.

[32] G. Smolker, Method and apparatus for protecting sensitive information contained in thin-film microelectonic circuitry, US Patent 3,882,323, May 6, **1975**.

[33] G.M. Fritz, C.H. Lam, D. Pfeiffer, K.P. Rodbell, and R.L. Wisnieff, Reactive material for integrated circuit tamper detection and response, US Patent 8,816,717, August 26 **2014**.

[34] C.W. Park, S.K. Kang, H.L. Hernandez, J.A. Kaitz, D.S. Wie, J. Shin, O.P. Lee, N.R. Sottos, J.S. Moore, and J.A. Rogers, Thermally triggered degradation of transient electronic devices. *Advanced Materials* 27(25), 3783-3788, **2015**.

[35] N. Banerjee, Y. Xie, H. Kim, and C.H. Mastrangelo, Microfluidic device for triggered chip transience. *IEEE SENSORS*, Baltimore, MD, USA, **2013**.

[36] N. Banerjee, Y. Xie, M.M. Rahman, H. Kim, and C.H. Mastrangelo, From chips to dust: The MEMS shatter secure chip. *IEEE MEMS*, San Fransisco, CA, USA, **2014**.

[37] S.S. Pandey and C.H. Mastrangelo, An exothermal energy release layer for microchip transience. *IEEE SENSORS*, Baltimore, MD, USA, **2013**.

[38] F. Keister and G. Smolker, Single layer self-destruct circuit produced by codeposition of tungstic oxide and aluminum, US Patent 3,742,120, June 26, **1973**.

[39] M.J. Moran, H.N. Shapiro, D.D. Boettner, and M.B. Bailey, Fundamentals of Engineering Thermodynamics. *John Wiley & Sons*, **2010**.

[40] R.R. Nellums, B.C. Terry, B.C. Tappan, S.F. Son, and L.J. Groven, Effect of solids loading on resonant mixed Al-Bi_2O_3 nanothermite powders. *Propellants, Explosives, Pyrotechnics* 38(5), 605-610, **2013**.

[41] A. Kosmala, R. Wright, Q. Zhang, and P. Kirby, Synthesis of silver nano particles and fabrication of aqueous Ag inks for inkjet printing. *Materials Chemistry and Physics* 129(3), 1075-1080, **2011**.

[42] H.H. Lee, K.S. Chou, and K.C. Huang, Inkjet printing of nanosized silver colloids. *Nanotechnology* 16(10), 2436-2441, **2005**.

[43] R. Bury, B. Desmazieres, and C. Treiner, Interactions between poly (vinylpyrrolidone) and ionic surfactants at various solid/water interfaces: a calorimetric investigation. *Colloids and Surfaces A: Physicochemical and Engineering Aspects* 127(1), 113-124, **1997**.

[44] M.W. Beckstead, K. Puduppakkam, P. Thakre, and V. Yang, Modeling of combustion and ignition of solid-propellant ingredients. *Progress in Energy and Combustion Science* 33(6), 497-551, **2007**.